A Practical Pilot for Channel Estimation of OTFS

Sanoopkumar P. S., Arman Farhang
Department of Electronic & Electrical Engineering, Trinity College Dublin, Ireland
{pungayis, arman.farhang}@tcd.ie.

***Abstract*—The widely used embedded impulse pilot for channel estimation of orthogonal time frequency space modulation (OTFS) has a prohibitively large peak to average power ratio (PAPR). Hence, in this paper, we propose a novel embedded pilot with cyclic prefix (PCP) that has a significantly reduced PAPR compared to the impulse pilot. This is achieved by spreading the pilot power along the delay dimension using a constant amplitude Zadoff-Chu (ZC) sequence with a cyclic prefix (CP). We analytically derive upper bound PAPR expressions for the impulse pilot and the proposed PCP. Together with our numerical results, these upper bounds attest the significant PAPR improvement that is achieved by PCP. We also develop a two-stage channel estimation technique with a superior performance to the threshold-based channel estimation for the impulse pilot. At the first stage, the channel is estimated by a linear estimator under the assumption of the channel being locally linear time invariant over each time-slot within the OTFS block. Taking advantage of the benefits that are offered by the CP in our proposed pilot structure, we develop a low complexity least squares based estimator for implementation of the first stage. At the second stage, we use the channel estimate from the first stage and the generalized complex exponential basis expansion model (GCE-BEM) to accurately estimate the full channel. Finally, we numerically analyse and show the superior estimation performance of our proposed channel estimator for PCP to the threshold-based estimator for the impulse pilot.**

I. Introduction

Orthogonal time frequency space modulation (OTFS) has recently emerged as a strong candidate waveform for the sixth generation wireless systems (6G), [1]. OTFS is robust to the time-varying channel effects that are present in the new application areas such as autonomous driving, hyper-loop trains, and integrated terrestrial-satellite communication systems, [2]. OTFS deploys the delay-Doppler (DD) domain for data transmission. Then it spreads the data symbols onto the time frequency (TF) plane to take advantage of the full diversity gain of the time and frequency selective channel in high mobility scenarios.

To exploit the advantages offered by OTFS, availability of accurate channel state information at the receiver is crucial. Hence, several channel estimation techniques for OTFS have recently emerged, [3]–[9]. In [3], a threshold-based channel estimation method was proposed. This method utilizes an embedded impulse pilot along with data that has a large power and is widely used for channel estimation and synchronisation in OTFS literature, [7]–[10]. More recently, in [11], a spline interpolation step in addition to the threshold-based estimation of [3] was proposed to improve the channel estimation accuracy. Embedded pilot sequences that spread the pilot power in both delay and Doppler dimensions, surrounded by zero guards, were proposed in [12] and [13] for channel estimation. However, the main issue associated with these pilot structures is their large peak to average power ratio (PAPR), [3], [13]. This is due to both the high power of the pilot and the zero guards surrounding it, [14], [15].

As another class of pilot structures for OTFS, superimposed pilots over the entire data symbols in DD domain were proposed in [4] and [16]. The main issue with this class is the need for sophisticated channel estimation and data detection, due to the interference between the data and pilot signal. Furthermore, the large power of the superimposed pilots adversely affect the PAPR performance. Preamble-based pilots are also deployed for channel estimation in OTFS, [5], [6]. However, the channel estimate becomes outdated in the data detection phase, i.e., after channel estimation in the preamble phase.

Accordingly, the existing channel estimation methods for OTFS either use pilots with prohibitively large PAPR or preamble-based pilots suffering from the channel ageing issue. Hence, in this paper, we propose a novel embedded pilot structure with a significantly reduced PAPR compared to the widely used impulse pilot. To tackle the PAPR issue, we start from in-depth PAPR analysis of the embedded impulse pilot. We analytically derive the PAPR upper bound for the impulse pilot that reveals the effect of the pilot parameters on the PAPR. This analysis provides us with valuable insights that lead to the development of our proposed pilot structure. In the proposed pilot structure, we spread the pilot power only along the delay dimension using a constant amplitude Zadoff-Chu (ZC) sequence. To avoid interference from data, we use a cyclic prefix (CP) instead of the zero guards. Hence, we introduce the novel concept of the pilot with a cyclic prefix (PCP) that not only eliminates the interference from data symbols to pilot, but it also reduces the PAPR of the OTFS signal. We also derive the PAPR upper bound expression for the proposed PCP that represents a significant PAPR reduction compared to the impulse pilot.

Based on the proposed PCP, we develop a two-stage channel estimation technique, which outperforms the threshold-based channel estimator with spline interpolation in [11]. At the first stage, we propose a linear channel estimator based on the least square (LS) or minimum mean squared error (MMSE) criterion. The channel estimate in Stage 1 is obtained assuming locally linear time invariant (LTI) channels over different time slots within the OTFS block. Using the initial estimate and the generalized complex exponential basis expansion model (GCE-BEM) [17], at the second stage, we estimate the time-variations within different time slots. Thanks to the presence of CP in our proposed pilot structure, we have developed a low complexity implementation for the proposed LS estimator. It is worth noting that the performance of the method in [11] can

This publication has emanated from research conducted with the financial support of Science Foundation Ireland under Grant number 19/FFP/7005(T).

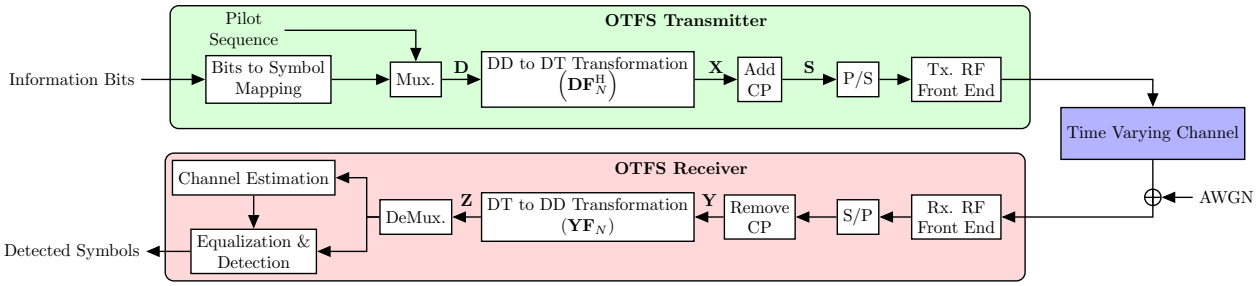

Fig. 1: Block diagram of the OTFS transceiver in baseband.

be substantially improved by replacing the spline interpolation step with Stage 2 of our proposed estimator. Finally, we numerically corroborate our claims as well as our analytical results through simulations. Based on our results, the proposed PCP has a substantially reduced PAPR compared with the impulse pilot, i.e., around 14 dB. Additionally, embedding the PCP along with data reduces the PAPR of the OTFS signal. Our simulation results also show the superior normalized mean square error (NMSE) performance of the proposed estimator to the one in [11]. Finally, the bit error rate (BER) results show that our proposed estimator provides a performance close to that of the perfectly known channel at the receiver.

Notations: In this paper, matrices, vectors and scalar quantities are denoted by boldface uppercase, boldface lowercase and normal letters, respectively. The Hermitian, transpose, Frobenius norm, and expected value operations are represented as $(\cdot)^{\mathrm{H}}$, $(\cdot)^{\mathrm{T}}$, $\|\cdot\|_{\mathrm{F}}$ and $\mathbb{E}\{\cdot\}$, respectively. The functions $\mathrm{circ}\{\mathbf{a}\}$ and $\mathrm{vec}\,(\mathbf{A})$ form a circulant matrix with the first column $\mathbf{a}$ and a vector by concatenating the columns of $\mathbf{A}$, respectively. $\circledast$, $\odot$, and $\oslash$ indicate the 2D circular convolution, Hadamard product and Hadamard division, respectively. $\mathbf{I}_M$ and $\mathbf{0}_{L\times K}$ denote the identity matrix of size M and the $L \times K$ zero matrix, respectively. $\mathbf{F}_N$ is the normalized N-point DFT matrix with the elements $F_N[p,q] = \frac{1}{\sqrt{N}} e^{-j\frac{2\pi pq}{N}}$ for $p, q = 0, \ldots, N-1$.

II. System Model

In this paper, we consider an OTFS system with M delay, N Doppler bins and the delay and Doppler resolution $\Delta\tau = T_{\mathrm{s}}$ and $\Delta\nu = \frac{1}{MNT_{\mathrm{s}}}$, respectively, where T_{s} is the sampling period. The quadrature amplitude modulated (QAM) data symbols together with the pilot signal are multiplexed on the corresponding DD bins to form the matrix $\mathbf{D} \in \mathbb{C}^{M\times N}$ with the elements $D[m,n]$ for $m = 0, \ldots, M-1$ and $n = 0, \ldots, N-1$. As the first step in OTFS modulation, the DD domain signal $\mathbf{D}$ is translated to the delay-time (DT) domain by taking N-point IDFT from its rows, i.e., $\mathbf{X} = \mathbf{DF}_N^{\mathrm{H}}$. Then, a cyclic prefix (CP) with the length M_{cp}, larger than the channel length L, is appended at the beginning of each column of the resulting DT domain matrix as

$$\mathbf{S} = \mathbf{A}_{\mathrm{cp}}\mathbf{X}, \tag{1}$$

where $\mathbf{A}_{\mathrm{cp}} = [\mathbf{G}_{\mathrm{cp}}^{\mathrm{T}}, \mathbf{I}_M^{\mathrm{T}}]^{\mathrm{T}}$ is the CP addition matrix and the $M_{\mathrm{cp}} \times M$ matrix $\mathbf{G}_{\mathrm{CP}}$ includes the last M_{cp} rows of the identity matrix $\mathbf{I}_M$. Finally, the signal $\mathbf{S}$ is passed through a parallel-to-serial converter (P/S), up-converted to the carrier frequency f_{c} and transmitted into the wireless channel.

After down-conversion to the baseband, serial-to-parallel conversion (S/P) and CP removal, the received DT domain signal can be expressed as $\mathbf{Y} = [\mathbf{y}_0, \ldots, \mathbf{y}_{N-1}]$ where

$$\mathbf{y}_n = \mathbf{R}_{\mathrm{cp}}\mathbf{H}_n\mathbf{A}_{\mathrm{cp}}\mathbf{x}_n + \mathbf{v}_n, \tag{2}$$

$\mathbf{v}_n \sim \mathcal{CN}(\mathbf{0}, \sigma_v^2\mathbf{I}_M)$ is the complex additive white Gaussian noise (AWGN) vector with the variance σ_v^2, $\mathbf{x}_n$ is the n^{th} column of $\mathbf{X}$, $\mathbf{H}_n$ is the linear time varying (LTV) channel matrix at time slot n, and $\mathbf{R}_{\mathrm{cp}} = [\mathbf{0}_{M\times M_{\mathrm{cp}}}, \mathbf{I}_M]$ is the CP removal matrix. Considering the channel gain for a given tap $\ell \in \{0, 1, \ldots, L-1\}$ at the sample index κ, $h[\kappa, \ell]$, the elements of $\mathbf{H}_n$ can be represented as $H_n[i,j] = h[n(M+M_{\mathrm{cp}})+i, i-j]$ for $i, j = 0, \ldots, M+M_{\mathrm{cp}}-1$. The received DD domain symbols can be obtained by taking N-point DFT from the rows of the received DT domain signal as $\mathbf{Z} = \mathbf{YF}_N$, [18]. Considering locally time invariant channels over different time slots, the elements of $\mathbf{Z}$ can be obtained from 2D circular convolution of the transmit symbols with the DD domain channel impulse response, [1], as

$$\mathbf{Z} = \mathbf{H}_{\mathrm{DD}} \circledast \mathbf{D} + \overline{\mathbf{V}}, \tag{3}$$

where $Z[m,n] = \sum_{l=0}^{M-1}\sum_{k=0}^{N-1} H_{\mathrm{DD}}[m-l, n-k]D[l,k] + \overline{V}[m,n]$, $\overline{V}[m,n]$'s are DD domain noise samples, i.e., the elements of $\overline{\mathbf{V}} = \mathbf{VF}_N$, $\mathbf{V} = [\mathbf{v}_0, \ldots, \mathbf{v}_{N-1}]$, and $H_{\mathrm{DD}}[m-l, n-k] = \frac{1}{N}\sum_{n'=0}^{N-1} H_{n'}[m,l]e^{-\frac{j2\pi n'(n-k)}{N}}$ is the DD domain channel response. Therefore, equation (3) can be represented in vectorized form as $\mathbf{z} = \mathbf{H}_{\mathrm{BC}}\mathbf{d} + \overline{\mathbf{v}}$ where $\mathbf{H}_{\mathrm{BC}} = (\mathbf{F}_N \otimes \mathbf{R}_{\mathrm{cp}})\,\mathbf{H}\,(\mathbf{F}_N^{\mathrm{H}} \otimes \mathbf{A}_{\mathrm{cp}})$, $\mathbf{z} = \mathrm{vec}(\mathbf{Z})$, $\mathbf{d} = \mathrm{vec}(\mathbf{D})$, and $\overline{\mathbf{v}} = \mathrm{vec}(\overline{\mathbf{V}})$. As it is shown in the OTFS transceiver block diagram in Fig. 1, after estimating the channel using the received pilot signal, the transmit data symbols are detected.

III. Proposed Pilot Structure

The widely used pilot for channel estimation in OTFS literature, [3], deploys a strong impulse at a given DD bin, $(m_{\mathrm{p}}, n_{\mathrm{p}})$. This pilot is surrounded by zero guards in $L-1$ delay and all the Doppler bins above and below it, see Fig. 2a. The zero guards are required to capture the channel response and avoid interference between the data symbols and the pilot. However, the large power of the impulse pilot results in an increased peak power and hence a large PAPR

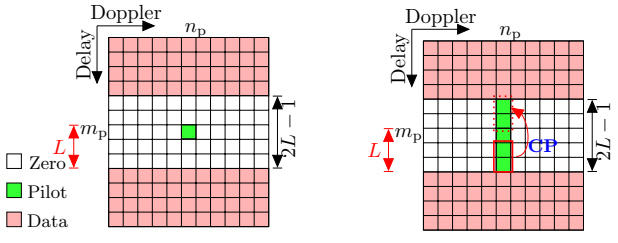

(a) Impulse Pilot (b) Proposed PCP

Fig. 2: Different pilot structures.

that is not favourable to practical systems. In the following, we analytically derive the upper bound expression for the PAPR of the OTFS signal with embedded impulse pilot[1]. This expression reveals the effect of the pilot parameters on the PAPR. Based on the insights that are gained from this analysis, we propose an embedded pilot structure that brings a substantial PAPR reduction compared to the impulse pilot.

The PAPR expression for the OTFS transmit signal is defined as,

$$\text{PAPR} = \frac{\max\limits_{m,n} \left\{|S[m,n]|^2\right\}}{P_{\text{avg}}}, \tag{4}$$

where $P_{\text{avg}} = \frac{1}{NM_{\text{T}}} \sum_{m=0}^{M_{\text{T}}-1} \sum_{n=0}^{N-1} \mathbb{E}\left\{|S[m,n]|^2\right\}$ represents the average signal power, and $M_{\text{T}} = M + M_{\text{cp}}$. $S[m,n]$'s are the elements of the matrix $\mathbf{S}$ in (1), $S[m+M_{\text{cp}},n] = \frac{1}{\sqrt{N}} \sum_{n'=0}^{N-1} D[m,n'] e^{j\frac{2\pi n n'}{N}}$ and $S[m_{\text{cp}},n] = S[m_{\text{cp}}+M,n]$ for $m_{\text{cp}} = 0,\ldots,M_{\text{cp}}-1$, $m = 0,\ldots,M-1$ and $n = 0,\ldots,N-1$. Since the transmit signal consists of both data and embedded pilot parts, P_{avg} can be expressed as $P_{\text{avg}} = \frac{1}{M_{\text{T}}N}(P_{\text{data}} + P_{\text{pilot}})$. The transmit data symbols $D[m,n']$ are taken from a given modulation alphabet, $\mathbb{A}$, and they are assumed to be i.i.d. random variables with zero mean and variance $\sigma_{\text{a}}^2 = \mathbb{E}\left\{|D[m,n']|^2\right\}$. Using Parsevel's theorem, $\sum_{n=0}^{N-1} \mathbb{E}\left\{|S[m,n]|^2\right\} = \sum_{n'=0}^{N-1} \mathbb{E}\left\{|D[m,n']|^2\right\}$, and $P_{\text{data}} = \sum_{m\in\Gamma_{\text{data}}} N\sigma_{\text{a}}^2 = N(M_{\text{T}}-(2L-1))\sigma_{\text{a}}^2$ where Γ_{data} is the set of the delay indices allocated to data. Hence, assuming $P_{\text{pilot}} = \gamma$,

$$P_{\text{avg}} = \frac{1}{NM_{\text{T}}}\left(N\left(M_{\text{T}}-(2L-1)\right)\sigma_{\text{a}}^2 + \gamma\right). \tag{5}$$

To find the upper bound for the PAPR of the impulse pilot, we expand $|S[m,n]|^2$ as $|\frac{1}{\sqrt{N}} \sum_{n'=0}^{N-1} D[m,n'] e^{j\frac{2\pi n n'}{N}}|^2$. Consequently, using the Cauchy-Schwarz inequality, we have $|S[m,n]|^2 \le \sum_{n'=0}^{N-1} |D[m,n']|^2$. Therefore,

$$\max_{m,n}\left\{|S[m,n]|^2\right\} \le \max_{m}\left\{\sum_{n'=0}^{N-1}|D[m,n']|^2\right\}. \tag{6}$$

If α is the maximum power of the modulated symbol in $\mathbb{A}$, for $m \in \Gamma_{\text{data}}$, $\max\limits_{m}\left\{\sum_{n'=0}^{N-1}|D[m,n']|^2\right\} = N\alpha$. When the impulse pilot is transformed into the DT domain, its power is evenly spread across time, in the delay bin m_{p}. Thus, for $m \in \Gamma_{\text{pilot}}$, where the set Γ_{pilot} includes the delay indices allocated to the pilot, $\max\limits_{m}\left\{\sum_{n'=0}^{N-1}|D[m,n']|^2\right\} = \gamma/N$. On this basis, we conclude that $\max\limits_{m,n}\left\{|S[m,n]|^2\right\} \le \max\left\{\gamma/N, N\alpha\right\}$. Finally, substituting this result and (5) into (4), an upper bound for the PAPR of the OTFS transmit signal with the embedded impulse pilot is obtained as

$$\text{PAPR}^{\text{Imp.}} \le \frac{M_{\text{T}}\max\left\{\gamma/N, N\alpha\right\}}{\left(M_{\text{T}}-2L+1\right)\sigma_{\text{a}}^2 + \gamma/N}. \tag{7}$$

To study the effect of the pilot on PAPR, we set the PAPR for the case where the whole DD plane is filled with data as a benchmark. In this case, $P_{\text{avg}} = \frac{1}{M_{\text{T}}N}P_{\text{data}} = \sigma_{\text{a}}^2$ and $\max\limits_{m,n}\left\{|S[m,n]|^2\right\} = N\alpha$ and thus,

$$\text{PAPR}^{\text{Full-Data}} \le N\alpha/\sigma_{\text{a}}^2. \tag{8}$$

This is the same as the upper bound derived in [20] for OTFS with the rectangular transmit pulse-shape. Comparing the upper bounds in (7) and (8), it can be seen that when $\gamma/N < N\alpha$ and $\gamma/N < (2L-1)\sigma_{\text{a}}^2$, the impulse pilot leads to a larger PAPR than the full-data case. This is while for $(2L-1)\sigma_{\text{a}}^2 < \gamma/N < N\alpha$, $\text{PAPR}^{\text{Imp.}} < \text{PAPR}^{\text{Full-Data}}$. As the relative pilot power with respect to data and thus, γ/N grows large, the PAPR of the impulse pilot is dominated by the pilot and it tends to the deterministic value of M_{T}. The latter is often the case, as it is the main requirement for accurate channel estimation using the threshold based estimator in [3]. Since, M_{T} is usually in the order of a couple of hundreds, PAPR becomes prohibitively large. As a result, the impulse pilot is not suitable for practical implementation of OTFS.

An interesting observation in the above analysis is the fact that the PAPR of the OTFS signal can be controlled by the embedded pilot and its parameters. In particular, as the pilot power grows large, the PAPR of the OTFS transmit signal is dominated by the pilot. However, the issue with the impulse pilot is the large peak power. To tackle this issue, one may decide to spread the pilot power to multiple delay and Doppler bins rather than concentrating all the pilot power in an impulse. From (6), it is evident that spreading the pilot power along the Doppler dimension does not have any effect on the peak power. This is while spreading the pilot power across multiple delay bins leads to peak power reduction. This creates a great opportunity to design a pilot that can reduce the PAPR of the OTFS transmit signal.

Based on the above discussion, we propose to distribute the pilot power γ along the delay bins that are allocated to the pilot on a given Doppler bin n_{p}. To protect the pilot against interference from data symbols due to the channel delay spread, a guard is required to be inserted between them. An option is to insert zero guards in $L-1$ delay and all the Doppler bins above the pilot. However, this does not allow to spread the pilot power across all the delay bins allocated to the pilot. Therefore, in our proposed pilot structure, we place a pilot sequence with length L on a given Doppler bin n_{p} and the delay bins $m_{\text{p}},\ldots,m_{\text{p}}+L-1$. Then, we append its last

[1]The PAPR derivations and analyses in this section are for the baseband signal. As the PAPR of the modulated bandpass signal can be simply found by addition of 3 dB to the PAPR of the baseband signal [19].

$L-1$ samples as a CP on the delay bins $m_{\rm p}-L,\ldots,m_{\rm p}-1$ so that it absorbs the interference from data symbols. This allows for spreading the pilot power γ over all the $2L-1$ delay bins. To minimize the peak power, in our proposed PCP, we deploy a constant amplitude sequence such as the widely utilized ZC sequence in wireless standards, e.g., 3GPP LTE and 5G NR, [21]. The proposed pilot structure is depicted in Fig. 2b.

Allocating the power of γ to our proposed pilot signal, the peak power can be calculated as $\max\limits_{m}\left\{\sum_{n'=0}^{N-1}|D[m,n']|^2\right\}=\frac{\gamma/N}{2L-1}$ for $m\in\Gamma_{\rm pilot}$. This is while the average power remains the same as (5). Consequently, the upper bound expression for the PAPR of the proposed pilot structure can be obtained as

$$\text{PAPR}^{\rm PCP}\leq\frac{M_{\rm T}\max\left\{\frac{\gamma/N}{2L-1},N\alpha\right\}}{(M_{\rm T}-2L+1)\,\sigma_{\rm a}^2+\gamma/N}. \tag{9}$$

Comparing (9) with (8), for $\frac{\gamma/N}{2L-1}<N\alpha$ and $\frac{\gamma/N}{2L-1}<\sigma_{\rm a}^2$, one may realize that $\text{PAPR}^{\rm PCP}>\text{PAPR}^{\rm Full-Data}$. This is while for $\sigma_{\rm a}^2<\frac{\gamma/N}{2L-1}<N\alpha$, $\text{PAPR}^{\rm PCP}<\text{PAPR}^{\rm Full-Data}$. An observation from (9), is that as the pilot power with respect to data and hence, $\frac{\gamma/N}{2L-1}$ grows large, $\text{PAPR}^{\rm PCP}$ tends to the deterministic value of $\frac{M_{\rm T}}{2L-1}$. This is a similar observation to the one we had for the impulse pilot. The difference here is that the PAPR for our proposed PCP is significantly reduced compared with the impulse pilot, i.e., $2L-1$ times. In 3GPP LTE and 5G NR standards, $M_{\rm cp}$ is chosen as 7% and in the extended CP case 25% the symbol duration. Considering $L=M_{\rm cp}$, as γ grows large, $\text{PAPR}^{\rm PCP}$ (in dB) tends to $10\log_{10}(\frac{1.07M}{0.14M-1})\approx 9$ dB and $10\log_{10}(\frac{1.25M}{0.5M-1})\approx 4$ dB for $M_{\rm cp}=0.07M$ and for $M_{\rm cp}=0.25M$, respectively.

In Fig. 3, we analyse the behaviour of the derived upper bound expressions in (7) and (9) with respect to γ while we compare them with the PAPR that is obtained from simulation. In our analysis, we consider $M=128$, $N=32$, $M_{\rm cp}=L=0.14M$, and $\sigma_{\rm a}^2=1$. Based on our results, for large values of γ, PAPR of both pilots becomes deterministic and coincides with the PAPR that is calculated using (7) and (9). This proves the validity of our derivations and discussions above. When γ takes smaller values, and the PAPR is dominated by data symbols, both pilot structures have the same performance for both PAPRs calculated using the derived upper bound expressions and simulations. However, as γ reaches a certain value, the PAPR for the impulse pilot dramatically increases, while the opposite is observed for our proposed pilot. For PCP, the PAPR from simulations decreases before it settles at $\frac{M_{\rm T}}{2L-1}$. This is because the peak power is still dominated by data symbols while the average power is increasing.

Based on the above, our proposed pilot structure has a substantially reduced PAPR compared with the impulse pilot. Furthermore, as will be discussed shortly, the proposed pilot structure has other attractive properties that facilitate simple channel estimation. Since the threshold-based channel estimation method in [3] is not applicable to PCP, in the following section, we propose a channel estimation technique that is suitable for both impulse and PCP pilot structures.

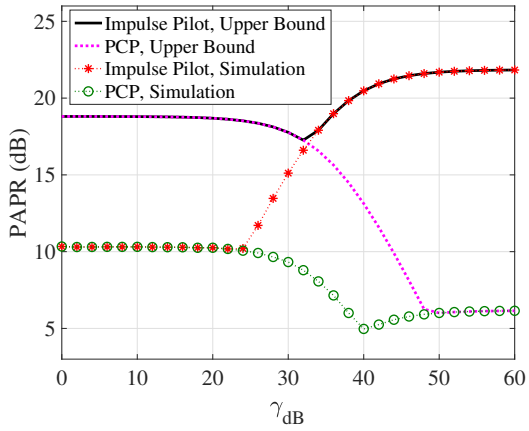

Fig. 3: PAPR vs. pilot power for PCP and impulse pilot.

IV. Proposed Channel Estimation Technique

In this section, we propose a two-stage channel estimation technique that is applicable to both PCP and impulse pilot structures. Assuming a locally LTI channel over each time slot, at the first stage of our proposed technique, we estimate the channel in the DD domain based on the LS or MMSE criterion. At the second stage, we capture the time variations of the channel within each time slot by fitting the channel estimates from the first stage to the basis expansion model. In the following, we explain this process in detail.

Stage 1: Considering locally LTI channel over different time slots, using (3), the received pilot signal in DD domain after discarding the CP can be obtained as

$$\mathbf{Z}_{\rm p}=\mathbf{D}_{\rm p}\circledast\mathbf{H}_{\rm DD}+\overline{\mathbf{V}}_{\rm p}, \tag{10}$$

where $\mathbf{D}_{\rm p}$ is the transmit pilot signal excluding the CP and $\overline{\mathbf{V}}_{\rm p}$ is the noise effect on the pilot with the elements $D_{\rm p}[i,n]=D[m_{\rm p}+i,n]$ and $\overline{V}_{\rm p}[i,n]=\overline{V}[m_{\rm p}+i,n]$ for $i=0,\ldots,L-1$ and $n=0,\ldots,N-1$, respectively. Equation (10) can be rearranged in vectorized form as

$$\mathbf{z}_{\rm p}=\boldsymbol{\mathcal{D}}_{\rm p}\mathbf{h}_{\rm DD}+\overline{\mathbf{v}}_{\rm p}, \tag{11}$$

where the matrix $\boldsymbol{\mathcal{D}}_{\rm p}=\text{circ}\{[\widetilde{\boldsymbol{\mathcal{D}}}_{{\rm p},0}^{\rm T},\ldots,\widetilde{\boldsymbol{\mathcal{D}}}_{{\rm p},N-1}^{\rm T}]^{\rm T}\}$ realizes the 2D circular convolution in (10), with the $L\times L$ circulant matrices $\widetilde{\boldsymbol{\mathcal{D}}}_{{\rm p},n}$ whose first columns are the $n^{\rm th}$ column of $\mathbf{D}_{\rm p}$, $\mathbf{h}_{\rm DD}=\text{vec}\{\mathbf{H}_{\rm DD}\}$, and $\overline{\mathbf{v}}_{\rm p}=\text{vec}\{\overline{\mathbf{V}}_{\rm p}\}$. Hence, from (11), $\mathbf{h}_{\rm DD}$ can be estimated using the LS or MMSE criterion, as

$$\widehat{\mathbf{h}}_{\rm DD}^{\rm LS}=\boldsymbol{\mathcal{D}}_{\rm p}^{-1}\mathbf{z}_{\rm p}, \tag{12}$$

or,

$$\widehat{\mathbf{h}}_{\rm DD}^{\rm MMSE}=\mathbf{C}_{h_{\rm DD}}\boldsymbol{\mathcal{D}}_{\rm p}^{\rm H}\left(\boldsymbol{\mathcal{D}}_{\rm p}\mathbf{C}_{h_{\rm DD}}\boldsymbol{\mathcal{D}}_{\rm p}^{\rm H}+\sigma_v^2\mathbf{I}_{NL}\right)^{-1}\mathbf{z}_{\rm p}, \tag{13}$$

respectively, where $\mathbf{C}_{h_{\rm DD}}=\mathbb{E}\{\mathbf{h}_{\rm DD}\mathbf{h}_{\rm DD}^{\rm H}\}$ is the correlation matrix of the DD domain channel response. Under the assumption of wide sense stationary and uncorrelated scattering (WSSUS) property, [17], $\mathbf{C}_{h_{\rm DD}}$ is a diagonal matrix with the elements

$$C_{h_{\rm DD}}[l,l]=\mathbb{E}\left\{|H_{\rm DD}[l,n]|^2\right\}. \tag{14}$$

Considering Rayleigh-distributed channel coefficients with Jakes Doppler spectrum, we have

$$\mathbb{E}\left\{h[\kappa_i,\ell_i]h^*[\kappa_j,\ell_j]\right\} = \rho_{\ell_i} J_0\left(2\pi f_{\mathrm{D}} T_{\mathrm{s}}(\kappa_i-\kappa_j)\right)\delta[\ell_i-\ell_j] \tag{15}$$

where, ρ_{ℓ_i} is the power of the channel tap ℓ_i and $\Sigma_{i=0}^{L-1}\rho_{\ell_i}=1$, f_{D} is the maximum Doppler shift, and $J_0(\cdot)$ is the zeroth order Bessel function of the first kind. Substituting $H_{\mathrm{DD}}[l,n] = \frac{1}{N}\sum_{n'=0}^{N-1} h[n'M_{\mathrm{T}}+l,n-l]e^{-j\frac{2\pi nn'}{N}}$ in (14) and using (15), the diagonal elements of $\mathbf{C}_{h_{\mathrm{DD}}}$ can be obtained as

$$C_{h_{\mathrm{DD}}}[l,l] = \sum_{p=-N}^{N} \frac{(N-|p|)}{N^2}\rho_l J_0(2\pi f_D T_s p M_{\mathrm{T}}) e^{-j\frac{2\pi pn}{N}}. \tag{16}$$

Stage 2: Our proposed linear estimators in (12) and (13) estimate the channel under the assumption of locally LTI channel over each time slot, i.e., every block of M_{T} samples. This is also the case for the threshold-based channel estimator in [3]. However, in practice, this assumption is not very accurate, [13], and the variations of the channel within the time slots are not captured using the aforementioned estimators. To tackle this issue, we take the channel estimates from Stage 1 to the delay-time domain and approximate the channel variations within each time slot using GCE-BEM by estimating the BEM coefficients. To this end, we first stack the consecutive elements of $\widehat{\mathbf{h}}_{\mathrm{DD}}^{\mathtt{LS}}$ or $\widehat{\mathbf{h}}_{\mathrm{DD}}^{\mathtt{MMSE}}$ in an $L\times N$ matrix $\widehat{\mathbf{H}}_{\mathrm{DD}}$[2]. Then, we take the DD domain channel estimate to the delay-time domain by taking N-point IDFT from its rows, i.e., $\widehat{\mathbf{H}}_{\mathrm{DT}} = \frac{1}{\sqrt{N}}\widehat{\mathbf{H}}_{\mathrm{DD}}\mathbf{F}_N^{\mathrm{H}}$. The estimates on the columns, n, of $\widehat{\mathbf{H}}_{\mathrm{DT}}$ can be thought of as the channel snapshots that are captured at time instants $\kappa\in\Psi=\{m_{\mathrm{p}}+M_{\mathrm{cp}}+nM_{\mathrm{T}}|n=0,\ldots,N-1\}$.

Using Q GCE basis functions, the complete DT domain channel can be expressed as [17],

$$\mathbf{H}_{\mathrm{DT}}^{\mathtt{Full}} = \mathbf{\Lambda}\mathbf{B}, \tag{17}$$

where $\mathbf{\Lambda}$ is the $L\times Q$ BEM coefficient matrix, and the $Q\times MN$ matrix $\mathbf{B}=[\mathbf{b}_0,\ldots,\mathbf{b}_{Q-1}]^{\mathrm{T}}$ includes the complex exponential basis vectors on its rows, i.e., $\mathbf{b}_q(n) = e^{\frac{j2\pi(q-Q/2)n}{KMN}}$, $\forall n\in\{iM_{\mathrm{T}}+M_{\mathrm{cp}},\ldots,iM_{\mathrm{T}}+M_{\mathrm{T}}-1\}$, $0\le i\le N-1$. For the GCE-BEM to accurately capture the time variations of the channel, the oversampling factor and number of basis functions are chosen as $K\ge 1$ and $Q=\lceil 2KM_{\mathrm{T}}Nf_{\mathrm{D}}T_{\mathrm{s}}\rceil+1$ [17]. Using (17), by stacking the columns of $\mathbf{B}$ with the indices $\kappa\in\Psi$ in ascending order to form the matrix $\mathbf{B}_\Psi$, the DT domain channel estimate from Stage 1 can be approximated as $\widehat{\mathbf{H}}_{\mathrm{DT}}=\mathbf{\Lambda}\mathbf{B}_\Psi$. Hence, the BEM coefficient matrix can be estimated as $\widehat{\mathbf{\Lambda}}=\widehat{\mathbf{H}}_{\mathrm{DT}}\mathbf{B}_\Psi^\dagger$

where $\mathbf{B}_\Psi^\dagger=\mathbf{B}_\Psi^{\mathrm{H}}(\mathbf{B}_\Psi\mathbf{B}_\Psi^{\mathrm{H}})^{-1}$ is the pseudo-inverse of $\mathbf{B}_\Psi$. Finally, the full channel can be estimated by substituting $\widehat{\mathbf{\Lambda}}$ into (17) as $\widehat{\mathbf{H}}_{\mathrm{DT}}^{\mathtt{Full}}=\widehat{\mathbf{\Lambda}}\mathbf{B}$ which can be simply translated back to the DD domain as $\widehat{\mathbf{H}}_{\mathrm{DD}}^{\mathtt{Full}}=\sqrt{N}\widehat{\mathbf{H}}_{\mathrm{DT}}^{\mathtt{Full}}\mathbf{F}_N$.

It is worth noting that Stage 2 is also applicable to the threshold-based channel estimation in [3]. Furthermore, Stage 2 can be thought of as an interpolation technique. Thus, in Section VI, we numerically analyze the MSE performance of our proposed channel estimation technique. We compare and show the superiority of our proposed technique over the threshold-based method in [3] and also the spline interpolation approach in [11] to estimate the full channel, $\mathbf{H}_{\mathrm{DD}}^{\mathtt{Full}}$.

[2]We have not used any superscript for $\mathbf{H}_{\mathrm{DD}}$ as both LS and MMSE estimates from Stage 1 can be considered as the input to Stage 2.

V. Low Complexity Implementation and Detection Considerations

In this section, we show that our proposed pilot structure facilitates a low complexity implementation of the LS estimator. Then, we provide a detailed complexity analysis of the channel estimators under study in terms of the number of complex multiplications (CMs). Finally, we discuss the considerations that need to be taken into account at data detection stage, as no guards are present in PCP between the pilot and data symbols.

From (10), one may realize that 2D circular convolution can be implemented by multiplication in the frequency-time (FT) domain. Consequently, the received FT domain pilot signal can be represented as

$$\mathbf{Z}_{\mathrm{p}}^{\mathrm{FT}} = \mathbf{D}_{\mathrm{p}}^{\mathrm{FT}}\odot\mathbf{H}_{\mathrm{FT}}+\overline{\mathbf{V}}_{\mathrm{p}}^{\mathrm{FT}}, \tag{18}$$

where $\mathbf{Z}_{\mathrm{p}}^{\mathrm{FT}}=\mathbf{F}_L\mathbf{Z}_{\mathrm{p}}\mathbf{F}_N^{\mathrm{H}}$, $\mathbf{D}_{\mathrm{p}}^{\mathrm{FT}}=\mathbf{F}_L\mathbf{D}_{\mathrm{p}}\mathbf{F}_N^{\mathrm{H}}$, and $\overline{\mathbf{V}}_{\mathrm{p}}^{\mathrm{FT}}=\mathbf{F}_L\overline{\mathbf{V}}_{\mathrm{p}}\mathbf{F}_N^{\mathrm{H}}$ are the FT domain counterparts of the corresponding DD domain signals in (10). It is worth noting that $\mathbf{Z}_{\mathrm{p}}^{\mathrm{FT}}$ can be directly calculated as $\mathbf{Z}_{\mathrm{p}}^{\mathrm{FT}}=\mathbf{F}_L\mathbf{Y}_{\mathrm{p}}$ where the $L\times N$ matrix $\mathbf{Y}_{\mathrm{p}}$ includes the DT domain received pilot after removing its CP. From (18), and using the known pilot signal at the receiver, the TF channel response can be estimated as

$$\widehat{\mathbf{H}}_{\mathrm{FT}} = \mathbf{Z}_{\mathrm{p}}^{\mathrm{FT}}\oslash\mathbf{D}_{\mathrm{p}}^{\mathrm{FT}}. \tag{19}$$

From (19), the DT domain channel estimate can be obtained as $\widehat{\mathbf{H}}_{\mathrm{DT}}=\frac{1}{\sqrt{L}}\mathbf{F}_L^{\mathrm{H}}\widehat{\mathbf{H}}_{\mathrm{FT}}$ and fed into Stage 2 of our proposed channel estimator to find $\widehat{\mathbf{H}}_{\mathrm{DD}}^{\mathtt{Full}}$.

Due to the presence of $\mathbf{C}_{h_{\mathrm{DD}}}$ in (13), the block circulant with circulant block structure of $\boldsymbol{\mathcal{D}}_{\mathrm{p}}$ is not retained in the matrices involved. Thus, low complexity implementation of the MMSE estimator in FT domain is impossible.

A. Computational Complexity Analysis

Table I summarizes the computational complexity of different channel estimators in terms of the number of CMs. Stage 2 of our proposed technique is considered in all the channel estimators under study, as it substantially improves the channel estimation accuracy. Computing the pseudo-inverse matrix $\mathbf{B}_\Psi^\dagger$ offline, Stage 2 channel estimation requires LNQ and $LQMN$ number of CMs to find $\widehat{\mathbf{\Lambda}}$ and $\widehat{\mathbf{H}}_{\mathrm{DD}}^{\mathtt{Full}}$, respectively.

As only one of the block matrices, i.e., $\widetilde{\boldsymbol{\mathcal{D}}}_{\mathrm{p},n_{\mathrm{p}}}$ forming $\boldsymbol{\mathcal{D}}_{\mathrm{p}}$ is non-zero and $\boldsymbol{\mathcal{D}}_{\mathrm{p}}^{-1}$ retains the block circulant structure of $\boldsymbol{\mathcal{D}}_{\mathrm{p}}$, direct implementation of the proposed LS estimator in (12), requires NL^2 number of CMs. The presence of the diagonal matrix $\mathbf{C}_{h_{\mathrm{DD}}}$ in (13) does not break the block structure of the matrices involved in the MMSE estimator. Thus, matrix inversion and multiplications for direct implementation of (13) require $\mathcal{O}(NL^3+2NL^2)$ number of CMs. As the input to Stage 2, the DD domain channel estimates from (12) and

TABLE I: Computational Complexity of Different Estimators.

Channel Estimator	Complex Multiplications (CMs)
LS Direct	$\mathcal{O}(NL^2 + \frac{LN}{2}\log_2 N + LNQ(M_{\mathrm{T}}+1))$
MMSE Direct	$\mathcal{O}(NL^3 + 2NL^2 + \frac{LN}{2}\log_2 N + LNQ(M_{\mathrm{T}}+1))$
Low complexity LS	$\mathcal{O}(NL\log_2 L + NL + LNQ(M_{\mathrm{T}}+1))$
Threshold-based	$\mathcal{O}(LN + LNQ(M+1))$

(13) should be converted to the DT domain. This requires L number of N-point DFT operations that can be efficiently implemented using the fast Fourier transform algorithm (FFT) with $\frac{LN}{2}\log_2 N$ number of CMs. The proposed low complexity implementation of the LS estimator in (19), requires the received signal to be taken to the FT domain and then a simple division[3] needs to be performed to find the FT channel estimate. Ultimately, the estimated channel is converted to the DT domain using N number of L-point DFT operations. Finally, the threshold-based channel estimator in [3] requires only LN complex division operations.

From Table I, it is evident that the threshold-based estimator in [3] has the lowest complexity. However, this estimator is not applicable to our proposed pilot structure with low PAPR as it was originally designed for the impulse pilot structure. To tackle this issue, we propose our low complexity LS estimator in this section with a computational load comparable to that of the threshold-based estimator.

B. Data Detection Considerations

To avoid spectral efficiency loss, in PCP, no guard is considered between pilot and data symbols. Due to the multipath effect, after the pilot goes through the channel, it interferes with data symbols. To tackle this issue, after the channel is estimated, the interference from pilot to data needs to be removed, otherwise, it can severely degrade the detection performance. Hence, the interference from pilot signal can be regenerated and subtracted from the received signal using the channel estimate $\widehat{\mathbf{H}}_{\mathrm{DD}}^{\mathtt{Full}}$. After removing the pilot, the resulting signal is fed to the OTFS detector.

VI. Simulation Results

In this section, we numerically analyze the PAPR performance of our proposed pilot structure, while comparing it with that of the fully loaded OTFS block with data as a benchmark and the impulse pilot. We also assess and compare our proposed channel estimator with the threshold-based method of [3] in terms of channel estimation NMSE, $\frac{\|\mathbf{H}_{\mathrm{DD}}^{\mathtt{Full}} - \widehat{\mathbf{H}}_{\mathrm{DD}}^{\mathtt{Full}}\|_{\mathrm{F}}^2}{\|\widehat{\mathbf{H}}_{\mathrm{DD}}^{\mathtt{Full}}\|_{\mathrm{F}}^2}$, and BER performance. We consider an OTFS system with $M = 128$ delay and $N = 32$ Doppler bins. The channel is simulated using the extended vehicular A (EVA) channel model, [22], at the carrier frequency of $f_{\mathrm{c}} = 5.9$ GHz, the sampling period of $T_{\mathrm{s}} = 133.33$ ns and the relative velocity of 500 km/h. For channel estimation with GCE-BEM, $Q = 7$ and $K = 2$ are chosen. In the BER analysis, we consider both 4-QAM (quadrature amplitude modulation) and 16-QAM.

[3]Complex division is considered to have the same complexity as complex multiplication.

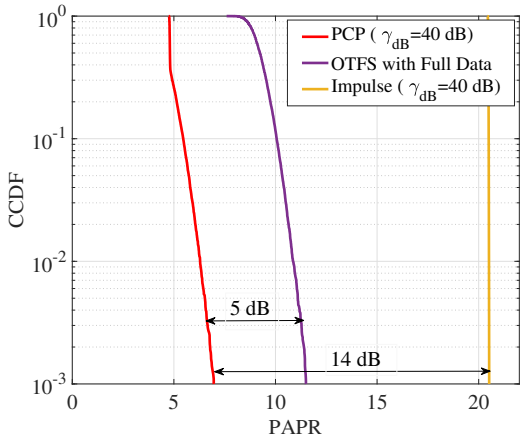

Fig. 4: PAPR performance comparison of OTFS with embedded impulse pilot, PCP and, full data for 16-OAM.

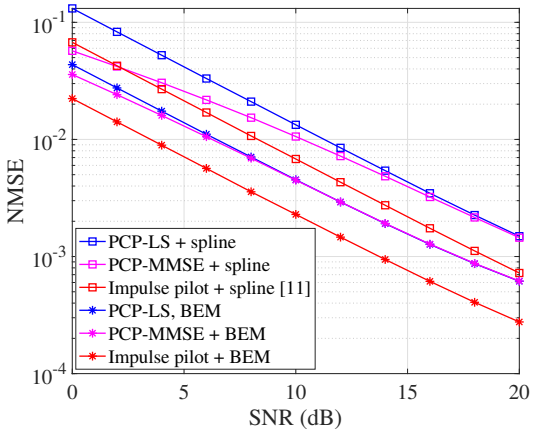

Fig. 5: NMSE performance comparison of different channel estimation techniques with different pilot structures.

Finally, we utilize the ZC sequence for PCP, while we set the pilot power at $\gamma_{\mathrm{dB}} = 40$ dB for both PCP and impulse pilot.

In Fig. 4, we analyze and compare the PAPR performance of our proposed PCP with that of the impulse pilot and our benchmark, i.e., fully loaded OTFS block with data. This shows that PCP not only has a substantially reduced PAPR compared with the impulse pilot, i.e., around 14 dB, but it also reduces the PAPR of the OTFS signal by around 5 dB.

To estimate $\widehat{\mathbf{H}}_{\mathrm{DD}}^{\mathtt{Full}}$ using the impulse pilot, threshold-based estimator followed by spline interpolation was proposed in [11]. However, as the threshold-based estimator is not suitable for PCP, we developed a two-stage channel estimator applicable to this pilot structure in Section IV. In Fig. 5, we have evaluated and shown the superior performance of our proposed technique compared with the method in [11]. As it is evident from our results, compared with spline interpolation, our proposed GCE-BEM based approach leads to the substantial performance improvement of around 5 dB for all the estimators under study. As it is shown in Fig. 5, the threshold-based method for the impulse pilot with our proposed GCE-BEM approach outperforms all the other techniques. However, the impulse pilot is not suitable for practical applications. Finally,

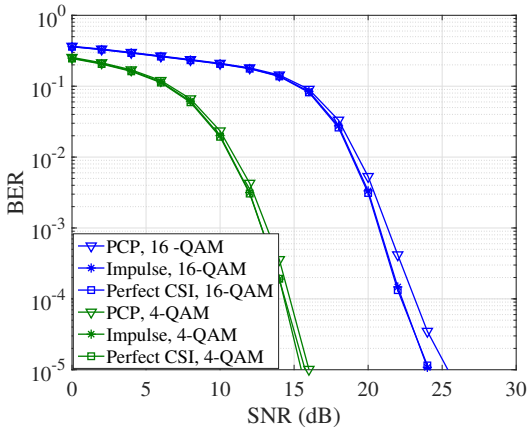

Fig. 6: BER performance comparison of different channel estimation techniques with different pilot structures.

it should be highlighted that the superiority of the MMSE to the LS estimator at low SNRs is negligible for the proposed GCE-BEM approach. Thus, given its low computational load and performance, we only consider the proposed LS estimator in our BER analysis in Fig. 6.

In Fig. 6, the BER performance of our proposed channel estimator for PCP and the threshold-based estimator in [11] for the impulse pilot are compared. In the method of [11], spline interpolation is replaced with Stage 2 of our proposed estimator. The results for both 4-QAM and 16-QAM are provided. For signal detection, the least squares minimum residual based technique with interference cancellation in [23] is deployed. From Fig. 6, it can be observed that our proposed estimator with PCP offers a BER performance very close to the perfect channel state information (CSI) case. The superior performance of the impulse pilot is due to the fact that the threshold-based estimator with Stage 2 of our proposed estimator provides more accurate channel estimates. However, the impulse pilot is not practical.

VII. Conclusion

In this paper, we developed an embedded pilot structure for OTFS with a significantly reduced PAPR compared to the widely used impulse pilot. This was shown both analytically and through numerical results. We derived upper bound expressions for the PAPR of the impulse pilot and the proposed PCP. In our pilot structure, we spread the pilot power across a constant amplitude ZC sequence along the delay dimension to reduce the PAPR. Furthermore, we proposed a two-stage channel estimation technique for PCP with a superior performance to the threshold-based estimator for the impulse pilot. In the first stage, the proposed estimator finds an initial channel estimate which is refined in its second stage. We showed that the threshold-based estimator followed by our proposed GCE-BEM approach improves the channel estimation accuracy when the impulse pilot is used. However, impulse pilot is not practical. Finally, we numerically analyzed the BER performance of our proposed channel estimator with PCP which led to a performance close to the perfect CSI case.

References

[1] R. Hadani, S. Rakib, M. Tsatsanis, A. Monk, A. J. Goldsmith, A. F. Molisch, and R. Calderbank, "Orthogonal Time Frequency Space Modulation," in *IEEE Wireless Commun. Netw. Conf. (WCNC)*, 2017, pp. 1–6.

[2] M. Noor-A-Rahim, Z. Liu, H. Lee, M. O. Khyam, J. He, D. Pesch, K. Moessner, W. Saad, and H. V. Poor, "6G for Vehicle-to-Everything (V2X) Communications: Enabling Technologies, Challenges, and Opportunities," *Proc. IEEE*, vol. 110, no. 6, pp. 712–734, 2022.

[3] P. Raviteja, K. T. Phan, and Y. Hong, "Embedded Pilot-Aided Channel Estimation for OTFS in Delay–Doppler Channels," *IEEE Trans. Veh. Technol.*, vol. 68, no. 5, pp. 4906–4917, 2019.

[4] W. Yuan, S. Li, Z. Wei, J. Yuan, and D. W. K. Ng, "Data-Aided Channel Estimation for OTFS Systems With a Superimposed Pilot and Data Transmission Scheme," *IEEE Wireless Commun. Lett.*, vol. 10, no. 9, pp. 1954–1958, 2021.

[5] K. R. Murali and A. Chockalingam, "On OTFS Modulation for High-Doppler Fading Channels," in *Inf. Theory and Appl. Workshop (ITA)*, 2018, pp. 1–10.

[6] O. K. Rasheed, G. D. Surabhi, and A. Chockalingam, "Sparse Delay-Doppler Channel Estimation in Rapidly Time-Varying Channels for Multiuser OTFS on the Uplink," in *IEEE Veh. Technol. Conf. (VTC)*, 2020, pp. 1–5.

[7] S. G. Neelam and P. R. Sahu, "Channel Estimation and Data detection of OTFS system in the presence of Receiver IQ Imbalance," in *2021 National Conf. Commun. (NCC)*, 2021, pp. 1–6.

[8] Y. Liu, Y. L. Guan, and D. G. G., "Near-Optimal BEM OTFS Receiver With Low Pilot Overhead for High-Mobility Communications," *IEEE Trans. Commun.*, vol. 70, no. 5, pp. 3392–3406, 2022.

[9] Y. Liu, S. Zhang, F. Gao, J. Ma, and X. Wang, "Uplink-Aided High Mobility Downlink Channel Estimation Over Massive MIMO-OTFS System," *IEEE J. Sel. Areas Commun.*, vol. 38, no. 9, pp. 1994–2009, 2020.

[10] M. Bayat and A. Farhang, "Time and Frequency Synchronization for OTFS," *IEEE Wireless Commun. Lett.*, pp. 1–1, 2022.

[11] T. Thaj, E. Viterbo, and Y. Hong, "Orthogonal Time Sequency Multiplexing Modulation: Analysis and Low-Complexity Receiver Design," *IEEE Trans. Wireless Commun.*, vol. 20, no. 12, pp. 7842–7855, 2021.

[12] W. Shen, L. Dai, J. An, P. Fan, and R. W. Heath, "Channel Estimation for Orthogonal Time Frequency Space (OTFS) Massive MIMO," *IEEE Trans. Signal Process.*, vol. 67, no. 16, pp. 4204–4217, 2019.

[13] H. Qu, G. Liu, L. Zhang, M. A. Imran, and S. Wen, "Low-Dimensional Subspace Estimation of Continuous-Doppler-Spread Channel in OTFS Systems," *IEEE Trans. Commun.*, vol. 69, no. 7, pp. 4717–4731, 2021.

[14] R. Marsalek, J. Blumenstein, A. Prokes, and T. Gotthans, "Orthogonal Time Frequency Space Modulation: Pilot Power Allocation and Nonlinear Power Amplifiers," in *IEEE Int. Symp. Signal Proces. Inf. Technol. (ISSPIT)*, 2019, pp. 1–4.

[15] S. Gao and J. Zheng, "Peak-to-Average Power Ratio Reduction in Pilot-Embedded OTFS Modulation Through Iterative Clipping and Filtering," *IEEE Commun. Lett.*, vol. 24, no. 9, pp. 2055–2059, 2020.

[16] H. B. Mishra, P. Singh, A. K. Prasad, and R. Budhiraja, "OTFS Channel Estimation and Data Detection Designs With Superimposed Pilots," *IEEE Trans. Wireless Commun.*, vol. 21, no. 4, pp. 2258–2274, 2022.

[17] F. Hlawatsch and G. Matz, *Wireless Communications over Rapidly Time-Varying Channels*. Academic Press, 2011.

[18] A. Farhang, A. RezazadehReyhani, L. E. Doyle, and B. Farhang-Boroujeny, "Low Complexity Modem Structure for OFDM-Based Orthogonal Time Frequency Space Modulation," *IEEE Wireless Commun. Lett.*, vol. 7, no. 3, pp. 344–347, 2018.

[19] T. J. Rouphael, *RF and Digital Signal processing for Software-defined radio*. Elsevier, 2008.

[20] G. D. Surabhi, R. M. Augustine, and A. Chockalingam, "Peak-to-Average Power Ratio of OTFS Modulation," *IEEE Commun. Lett.*, vol. 23, no. 6, pp. 999–1002, 2019.

[21] 3GPP, "5G;System architecture for the 5G System (Release 16)," *3rd Generation Partnership Project (3GPP)*, TS 123.501 V16.6.0, 2020.

[22] ——, "Evolved universal terrestrial radio access (E-UTRA); base station (BS) radio transmission and reception (Release 12)," *3rd Generation Partnership Project (3GPP)*, TS 36.104 V15.3.0, 2018.

[23] H. Qu, G. Liu, L. Zhang, S. Wen, and M. A. Imran, "Low-Complexity Symbol Detection and Interference Cancellation for OTFS System," *IEEE Trans. Commun.*, vol. 69, no. 3, pp. 1524–1537, 2021.